

# L-Arginine-Functionalized Pd–Ni Catalyst Enhances Direct H<sub>2</sub>O<sub>2</sub> Synthesis in Microreactors

Xuan Chen, Zheng Chen, Lang Wu, Feifei Hu, Xin Zhou, Qian Lin,\* Hongyan Pan,\* Yongyong Shi,\* and Donghai Jiang\*



Cite This: *Langmuir* 2025, 41, 12745–12756



Read Online

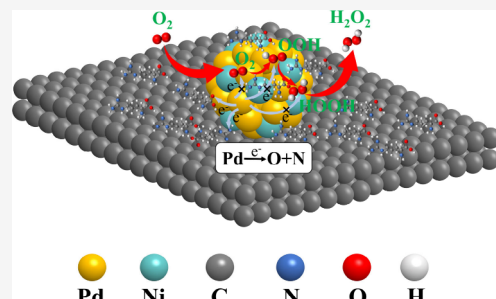
ACCESS |

Metrics & More

Article Recommendations

Supporting Information

**ABSTRACT:** Using an L-arginine (LA)-functionalized Pd–Ni catalyst, hydrogen peroxide (H<sub>2</sub>O<sub>2</sub>) was directly synthesized via a self-designed microreactor at ambient temperature and pressure. The yield of H<sub>2</sub>O<sub>2</sub> achieved 574.31 g kg<sub>cat</sub><sup>-1</sup> h<sup>-1</sup>, with the concentration of H<sub>2</sub>O<sub>2</sub> in the solution reaching 4.05 wt % per hour. After five cycles and online activation, the LA functionalized Pd–Ni catalyst maintained high H<sub>2</sub>O<sub>2</sub> catalytic activity. The catalytic activity evaluation experiments, characterization results, and simulation studies demonstrated that Ni doping and LA-functionalization synergistically modulate the electronic structure of the active Pd component. This modulation increases the concentration of Pd<sup>2+</sup> at the active sites, effectively inhibits the dissociation of the O–O bond in O<sub>2</sub><sup>\*</sup>, OOH<sup>\*</sup>, and HOOH<sup>\*</sup> species, thereby enhancing the catalytic performance for H<sub>2</sub>O<sub>2</sub> production. This study proposes a systematic strategy for the design of Pd-based catalysts to directly synthesize highly efficient H<sub>2</sub>O<sub>2</sub>.



## INTRODUCTION

As a crucial green chemical, H<sub>2</sub>O<sub>2</sub> has found extensive applications in pulp bleaching, wastewater treatment, the textile industry, chemical synthesis, metallurgy, aerospace, and the electronics sector. Consequently, the demand for H<sub>2</sub>O<sub>2</sub> has been increasing annually.<sup>1–3</sup> Currently, over 95% of global H<sub>2</sub>O<sub>2</sub> production relies on the anthraquinone process (AO). However, this method has notable drawbacks, including substantial capital investment requirements, significant environmental pollution, and elevated risks associated with the transportation of high-concentration H<sub>2</sub>O<sub>2</sub>.<sup>4–6</sup> Simultaneously, over two-thirds of H<sub>2</sub>O<sub>2</sub> applications require concentrations of less than 9 wt %.<sup>7,8</sup> Therefore, it is imperative to develop an economically viable, environmentally friendly, safe, and readily available method to replace the AO-based production of H<sub>2</sub>O<sub>2</sub>. The direct synthesis of H<sub>2</sub>O<sub>2</sub> (DSHP) from hydrogen (H<sub>2</sub>) and oxygen (O<sub>2</sub>) using Pd as the active component at room temperature represents a promising alternative to the AO process for H<sub>2</sub>O<sub>2</sub> production. This method offers several advantages, including atomic economy, the use of environmentally benign solvents such as methanol or water, the absence of hazardous organic compounds, suitability for small-scale production, and ease of integration with downstream processes.<sup>9–11</sup> However, the primary limitation of the DSHP process lies in the suboptimal catalytic activity, selectivity, and stability of the Pd catalyst, which significantly hinders its industrial application. Therefore, conducting research on the rational design and controllable preparation of Pd catalysts

with high catalytic activity, high selectivity, and stability holds significant practical and theoretical value.<sup>12–14</sup>

The irreversible dissociation of the O–O bond in species such as O<sub>2</sub><sup>\*</sup>, OOH<sup>\*</sup>, and HOOH<sup>\*</sup> is primarily attributed to the electron transfer from the active component of the Pd catalyst to these adsorbed species at the active site. This process is the main reason for the decrease in H<sub>2</sub>O<sub>2</sub> selectivity and yield.<sup>15</sup> To suppress the dissociation of O–O bonds and enhance the yield and selectivity of H<sub>2</sub>O<sub>2</sub>, a secondary metal is commonly incorporated into Pd-based catalysts to improve their catalytic performance. Common combinations include Pd–Pt,<sup>16</sup> Pd–Au,<sup>17</sup> Pd–Ag<sup>18</sup> among others. By modulating the electronic structure of Pd through the incorporation of precious metals and effectively suppressing the dissociation of O–O bonds, the yield and selectivity of H<sub>2</sub>O<sub>2</sub> production can be significantly enhanced. However, the incorporation of precious metals is prohibitively expensive and poses significant challenges for industrial application. Therefore, it is essential for DSHP to modulate the electronic structure of Pd by incorporating nonprecious metals, thereby enhancing the catalytic activity of the catalyst, suppressing O–O bond dissociation, improving the yield and selectivity of H<sub>2</sub>O<sub>2</sub>.

Received: February 27, 2025

Revised: May 7, 2025

Accepted: May 8, 2025

Published: May 14, 2025



production, and reducing costs. For instance, Pd–Sn,<sup>19</sup> Pd–Sb,<sup>20</sup> Pd–Co,<sup>21</sup> Pd–Ga and Pd–In.<sup>22</sup> Although the incorporation of these nonprecious metals successfully suppressed the dissociation of O–O bonds, it only enhanced either the yield, selectivity, or concentration of H<sub>2</sub>O<sub>2</sub>, or the conversion rate of H<sub>2</sub>, but not all of them simultaneously. Existing studies have demonstrated that incorporating Ni into Pd-based catalysts can substantially enhance the yield, selectivity, and stability of H<sub>2</sub>O<sub>2</sub> production. Maity et al. incorporated Ni into the Pd-based catalyst, achieving a selectivity as high as 95% for H<sub>2</sub>O<sub>2</sub> production. The catalytic activity of the Ni–Pd catalyst was 3-fold higher than that of the single Pd catalyst. Moreover, the Ni–Pd catalyst exhibited excellent stability under harsh conditions, even in the presence of HCl and Br<sup>−</sup>.<sup>23</sup> Feng et al. doped Ni into the material, achieving high catalytic activity, excellent selectivity and stability, as well as effectively suppressing H<sub>2</sub>O<sub>2</sub> decomposition.<sup>24</sup> The incorporation of Ni effectively modulates the electronic structure of Pd, suppresses O–O bond dissociation, and significantly enhances the catalytic activity, stability, yield, and selectivity for H<sub>2</sub>O<sub>2</sub> production. Given its abundant reserves, Ni serves as an ideal nonprecious metal dopant for Pd-based catalysts.

In recent years, the application of ligands to modulate the electronic structure of Pd and suppress O–O bond dissociation has significantly enhanced the yield and selectivity of H<sub>2</sub>O<sub>2</sub> production, as well as the activity and stability of the catalyst.<sup>25–27</sup> The electronic structure of Pd was modified through the introduction of N-heterocyclic carbene (NHC), resulting in the production of 5442.35 g kg<sub>cat</sub><sup>−1</sup> h<sup>−1</sup> of H<sub>2</sub>O<sub>2</sub>.<sup>28</sup> However, the concentration of H<sub>2</sub>O<sub>2</sub> produced was relatively low (<1 wt %), which is significantly lower than the concentration required for direct application (3–9 wt %). Amino acids (AA) are organic compounds composed of C, N, and O, among other elements. The functional groups within amino acids play a crucial role in modulating the electronic structure of metal active sites, promoting the dispersion of metal active components, and enhancing both the activity and stability of catalysts. For instance, the study conducted by Yang et al. revealed that the functional modification of glycine not only substantially improved the dispersibility of Ni but also effectively decreased its particle size.<sup>29</sup> Studies have demonstrated that the functional groups of L-lysine, specifically the carboxyl (−COO<sup>−</sup>) and amino (−NH<sub>2</sub>) groups, are crucial for facilitating electron transfer.<sup>30</sup> The research conducted by Jiang et al. demonstrates that the functional modification of LA effectively modulates the electronic structure of Pd. The functional groups present in LA, such as −COO<sup>−</sup> and −NH<sub>2</sub>, can form amide bonds, hydrogen bonds, and covalent bonds with the functional groups on the carbon carrier (AC), thereby enhancing the stability of the catalyst.<sup>31</sup> Although LA has not yet been applied in DSHP, it is an amino acid substance that contains functional groups similar to those of other amino acids, such as glycine and L-lysine. The functional modification of LA can effectively regulate the electronic structure of Pd, enhance the dispersion of metal active components, reduce the size of metal particles, and improve the stability of the catalyst. Therefore, LA serves as an ideal ligand for the functional modification of metal active components and supports in DSHP reactions.

DSHP is limited by the relatively high explosion risk associated with the direct mixing of H<sub>2</sub> and O<sub>2</sub>. In contrast, microreactors offer rapid heat dissipation, improved mass transfer, and effectively mitigate the explosion risk inherent in

the direct mixing of H<sub>2</sub> and O<sub>2</sub>.<sup>32</sup> It is widely favored by numerous researchers in the DSHP field. For instance, the Inoue research group successfully employed microreactors in DSHP, enabling safe and direct mixing of H<sub>2</sub> and O<sub>2</sub> within the explosive limit, ensuring proper gas–liquid distribution, and achieving the synthesis of H<sub>2</sub>O<sub>2</sub> at a higher concentration.<sup>32–34</sup> However, the reaction must be conducted under a high pressure ranging from 2 to 3 MPa, which imposes stricter demands on the material selection for the microreactor. Kanungo et al. immobilized Au Pd nanoparticles on the inner wall of the channel within the microreactor for DSHP, enabling the synthesis of H<sub>2</sub>O<sub>2</sub> at a concentration of 1.8 wt %.<sup>35</sup> Since the catalyst is immobilized on the inner wall of the channel in the microreactor, its deactivation necessitates replacing the entire microreactor, which incurs prohibitively high costs. Yang et al. designed a microreactor for the synthesis of H<sub>2</sub>O<sub>2</sub> at a concentration of 0.388 wt % under normal pressure. The continuous flow operation minimized the contact time between H<sub>2</sub>O<sub>2</sub> and the catalyst, thereby reducing the decomposition of H<sub>2</sub>O<sub>2</sub> induced by the catalyst. Consequently, the produced H<sub>2</sub>O<sub>2</sub> could be utilized directly without further processing.<sup>36</sup> However, the concentration of H<sub>2</sub>O<sub>2</sub> generated remains relatively low. Therefore, it is essential to develop microreactors capable of continuously producing high-concentration H<sub>2</sub>O<sub>2</sub> under normal temperature and pressure conditions, thereby enabling low-cost, on-site production and facilitating the industrial implementation of DSHP.

In summary, this paper describes the independent design and fabrication of a microreactor for use as a DSHP reactor, utilizing LA-functionalized Pd–Ni catalyst and poly(methyl methacrylate) (PMMA) as key materials. The impact of Ni doped and LA-functionalized Pd catalysts on the selectivity, yield, and concentration of H<sub>2</sub>O<sub>2</sub> was investigated through experimental methods, DFT calculations, and comprehensive studies. The conclusions of this study offer valuable insights and serve as a reference for the future design and development of catalysts and microreactors.

## EXPERIMENTAL SECTION

**Investigational Pharmaceuticals.** Palladium chloride (PdCl<sub>2</sub>, 60.0%) and methanol (CH<sub>3</sub>OH, 99.5%) were procured from Chengdu Jinshan Chemical Reagent Co., Ltd. Nickel chloride hexahydrate (NiCl<sub>2</sub>·6H<sub>2</sub>O, 98.0%) was procured from Tianjin Zhiyuan Chemical Reagent Co., Ltd. L-Arginine (C<sub>6</sub>H<sub>14</sub>N<sub>4</sub>O<sub>2</sub>, 99%) was procured from Shanghai Adamas Reagent Co., Ltd. Sodium borohydride (NaBH<sub>4</sub>, 96%) was procured from Sinopharm Chemical Reagent Co., Ltd. Sodium bromide (NaBr, 99%) was obtained from Shanghai Aladdin Biochemical Technology Co., Ltd. Hydrogen peroxide (H<sub>2</sub>O<sub>2</sub>, wt = 30.0%) and sulfuric acid (H<sub>2</sub>SO<sub>4</sub>, 98.0%) were procured from Chongqing Chuandong Chemical Co., Ltd. The activated carbon (AC) used in this study was procured from Fujian Yuanli Activated Carbon Co., Ltd. All experimental reagents are of analytical grade and are ready for use without additional purification. Deionized water was utilized exclusively in all stages of the experiment.

**Preparation of Catalysts.** The preparation of Pd–Ni/AC-LA is illustrated in Figure 1. Specifically, 0.1 g of AC was placed in a beaker. Subsequently, 126.6 μL of 0.075 M H<sub>2</sub>PdCl<sub>4</sub> solution, 12.7 μL of 0.075 M NiCl<sub>2</sub> solution, 10 mg of LA, and 1.5 mL of deionized water were sequentially added. The mixture was then transferred to a constant temperature shaker and oscillated at 25 °C for 7 h. Then, 1.015 M of freshly prepared sodium borohydride solution was added, and the mixture was continuously oscillated and reduced at 25 °C in a constant temperature shaker for 7 h. The sample was washed, filtered

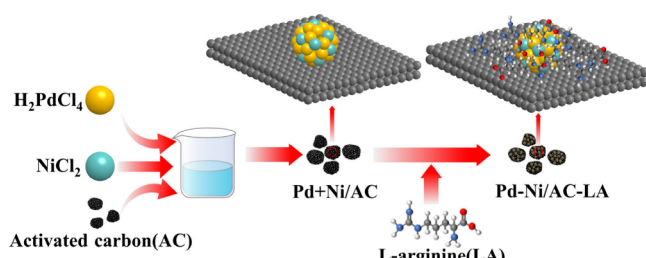


**Figure 1.** Schematic illustration of the preparation process for Pd-Ni/AC-LA.

to neutrality, and dried in a vacuum oven at 80 °C for 12 h to obtain Pd-Ni/AC-LA (Ni:Pd = 0.1, LA = 10 mg). Additionally, Pd/AC, Pd/AC-LA (LA = 10 mg), and Pd-Ni/AC (Ni:Pd = 0.1) were prepared using the same procedure. Pd-Ni/AC (Ni:Pd = 0.04, 0.06, 0.08, 0.12, and 0.14) series catalysts were prepared by varying the Ni content. Additionally, Pd-Ni/AC-LA catalysts (Ni:Pd = 0.10, LA = 5, 15, 20, and 25 mg) were synthesized to investigate the effects of Ni/Pd ratio and LA loading on H<sub>2</sub>O<sub>2</sub> yield. The metal content of the prepared catalyst was quantified by ICP-MS, and the results were in good agreement with the theoretically calculated molar ratios of Pd and Ni (Table S1).

**Catalyst Characterization.** Transmission electron microscopy (TEM, Tecnai G2 F20, Thermo Fisher, USA) was employed to characterize the morphology of the catalyst and determine the particle size of the active components. Physical adsorption instrument (BET, Micrometrics ASAP 2020, McKesson Corporation, USA) was used to study the specific surface area (SBET), pore volume and pore size distribution of carbon carriers. The surface composition and chemical state of the catalyst were studied by X-ray photoelectron spectroscopy (XPS, K-Alpha Plus, Thermo Fisher, USA). The functional groups of the catalysts were characterized using Fourier transform infrared spectroscopy (FT-IR, Nicolet iS50, Thermo Fisher, USA). Raman spectrometers (Raman, LabRAM Aramis, France) were employed to characterize the degree of graphitization and defect density of the carbon carriers. The crystal phase of the catalyst was determined by X-ray powder diffraction (XRD, D8 Advance, Bruker, Germany). The adsorption capacities of H<sub>2</sub> and O<sub>2</sub> were investigated using a chemical adsorption analyzer (TPD, Auto Chem II 2920, Micromeritics Instrument Corporation, USA). The Pd and Ni content in the catalysts was quantified using inductively coupled plasma mass spectrometry (ICP-MS, PerkinElmer, USA).

**Comprehensive Evaluation of Catalytic Performance.** The microreactor comprises a PMMA substrate (40.5 mm × 60.5 mm × 3.8 mm) featuring all microchannels and inlet/outlet ports (diameter: 1.3 mm), along with a Teflon sheet serving as a gasket. All microchannels on the PMMA substrate are precisely machined and engraved using a CNC machine (Seiken Instruments Desktop CNC 3040). The machined PMMA sheets, along with Teflon sheets, are then assembled onto a custom fixture equipped with connecting fittings for attachment to external piping, as illustrated in Figure 2.

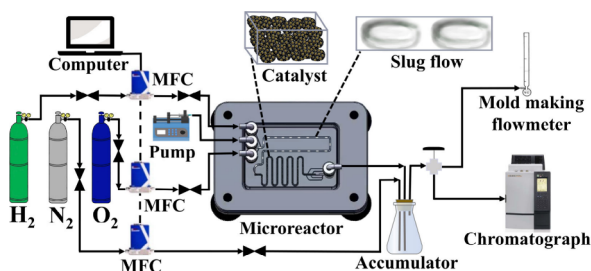


**Figure 2.** Schematic representation of the microreactor experimental setup for the direct synthesis of H<sub>2</sub>O<sub>2</sub> from H<sub>2</sub> and O<sub>2</sub>.

The microreactor is equipped with three inlet ports for H<sub>2</sub>, O<sub>2</sub>, and the solvent, a single outlet port, a gas–liquid mixing zone, a packed bed section, and six DAMS units to prevent catalyst backflow into the gas–liquid mixing zone and out of the microreactor. The width of the gas–liquid inlet is 200 μm, with a depth of 250 μm. The gas mixing channel and the filler bed channel, both 800 μm in depth and width, are interconnected by a dam measuring 2000 μm in length, 800 μm in width, and 100 μm in depth. The dam, which is smaller than the catalyst particles, is positioned at the entrance of the catalyst inlet to prevent backflow of catalyst particles into the gas mixing zone during filling. Additionally, five dams of identical size are situated at the outlet to trap any catalyst particles. The fluid flow rate is controlled by a high-precision injection pump (LD-P2020, Shanghai Lande Medical Instruments Co., Ltd., China) in conjunction with a 30 mL syringe (BD Plastic, Jiangxi Fenglin Medical Instruments Co., Ltd., China). The gas flow rate is regulated by a mass flow controller (MFC model CS200A, Beijing Seven Star Huachuang Electronics Co., Ltd., China). Prior to use, nitrogen (N<sub>2</sub>) is employed to test the microreactor for leaks. Following this, the reaction mixture (CH<sub>3</sub>OH + H<sub>2</sub>SO<sub>4</sub> + NaBr) undergoes acidification for 30 min. Subsequently, H<sub>2</sub> at a flow rate of 2.88 mL min<sup>-1</sup> and O<sub>2</sub> at a flow rate of 4.12 mL min<sup>-1</sup> are introduced into the system for the reaction. Meanwhile, N<sub>2</sub> flows directly into the H<sub>2</sub>O<sub>2</sub> collection vessel at a rate of 10 mL min<sup>-1</sup>, serving as a protective gas. The flow rate of the tail gas was measured using a precision molding flowmeter, and the concentrations of H<sub>2</sub> and O<sub>2</sub> in the tail gas were analyzed by gas chromatography (GC-7820). A Teflon tube served as the connecting conduit, and the reaction occurred under ambient temperature and pressure conditions.

The concentration of H<sub>2</sub>O<sub>2</sub> in the reaction medium was determined by iodometric titration. Using this data, the H<sub>2</sub> conversion (%), H<sub>2</sub>O<sub>2</sub> selectivity (%), and H<sub>2</sub>O<sub>2</sub> yield (g kg<sub>cat</sub><sup>-1</sup> h<sup>-1</sup>) of the catalyst were calculated according to eqs 1, 2, and 3.

$$\text{H}_2\text{O}_2 \text{ productivity} = \frac{n(\text{H}_2\text{O}_2)_{\text{detected}}}{m_{\text{cat}} \times t_{\text{reaction}}} \quad (1)$$

$$\text{H}_2\text{O}_2 \text{ selectivity} = \frac{n(\text{H}_2\text{O}_2)_{\text{detected}}}{n(\text{H}_2)_{\text{reacted}}} \times 100\% \quad (2)$$

$$\text{H}_2 \text{ conversion} = \frac{n(\text{H}_2)_{\text{in}} - n(\text{H}_2)_{\text{out}}}{n(\text{H}_2)_{\text{in}}} \times 100\% \quad (3)$$

Hydrogenation and decomposition experiments of the catalysts were conducted in the aforementioned microreactor using the same reaction medium, supplemented with 200.0 μL of a 30.0 wt % H<sub>2</sub>O<sub>2</sub> solution. Hydrogenation experiments were conducted under H<sub>2</sub> and N<sub>2</sub> atmospheres with flow rates of 2.88 mL min<sup>-1</sup> and 10.0 mL min<sup>-1</sup>, respectively. For the decomposition experiment, only N<sub>2</sub> (10.0 mL min<sup>-1</sup>) was injected. The H<sub>2</sub>O<sub>2</sub> hydrogenation or decomposition rate of the catalyst (g kg<sub>cat</sub><sup>-1</sup> h<sup>-1</sup>) was calculated by eq 4.

#### H<sub>2</sub>O<sub>2</sub> Hydrogenation and Decomposition rate

$$= \frac{n(\text{H}_2\text{O}_2)_{\text{before}} - n(\text{H}_2\text{O}_2)_{\text{after}}}{m_{\text{cat}} \times t_{\text{reaction}}} \quad (4)$$

**Cycle experiment:** The 20 mg catalyst was put into the microreactor, acidified with the reaction solution at 25 °C for 30 min, and then injected with H<sub>2</sub> (2.88 mL min<sup>-1</sup>) and O<sub>2</sub> (4.12 mL min<sup>-1</sup>) for reaction, and N<sub>2</sub> (10 mL min<sup>-1</sup>) was directly injected into the H<sub>2</sub>O<sub>2</sub> collection bottle as a protective gas. The concentrations of H<sub>2</sub> and O<sub>2</sub> in the tail gas were analyzed using gas chromatography (GC-7820), while the yield and concentration of H<sub>2</sub>O<sub>2</sub> in the reaction medium were determined through iodometric titration. After the reaction, the catalyst recovered from the microreactor was sequentially washed, filtered to neutrality, and dried under vacuum at 80 °C for 12 h. The dried catalyst was subsequently weighed, and the next cycle of experiments was initiated.

**DFT Calculation.** All periodic spin-polarized DFT calculations were conducted using the Vienna Ab initio Simulation Package

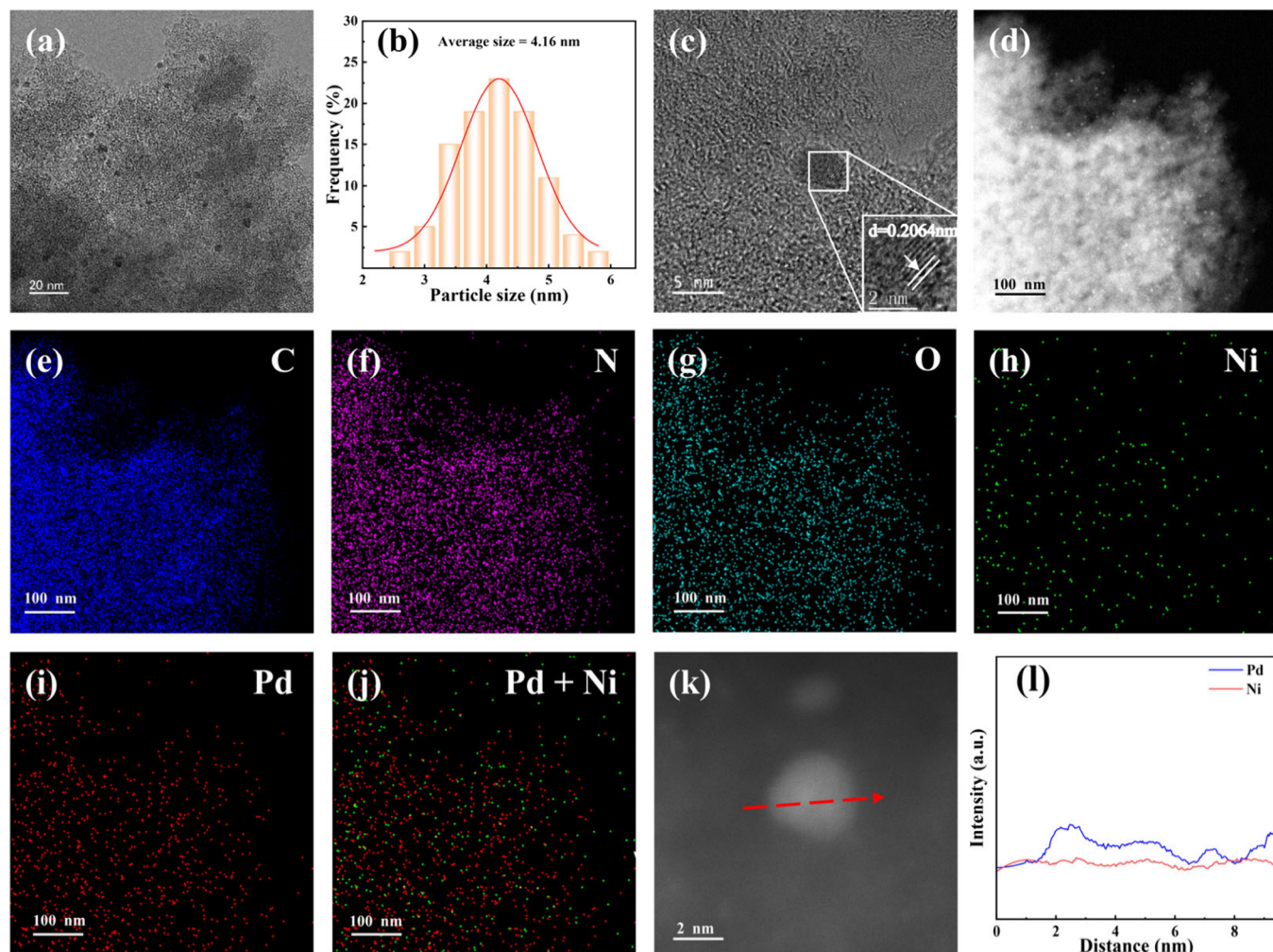


**Figure 3.** (a and b) TEM images and particle size distributions of Pd-Ni/AC-LA catalysts. (c) HRTEM image of Pd nanoparticles in the Pd-Ni/AC-LA catalyst. (d) ~ (j) HAADF-STEM images of the Pd-Ni/AC-LA catalyst and corresponding mapping images of C, N, O, Pd, Ni and Pd + Ni. (k) and (l) EDX line scan analysis.

(VASP), which was developed at the University of Vienna.<sup>37,38</sup> The electron exchange and correlation effects can be accurately described using the generalized gradient approximation (GGA) with the Perdew–Burke–Ernzerhof (PBE) functional.<sup>39</sup> The interaction between the atomic nucleus and valence electrons is described using the projector augmented wave (PAW) method.<sup>40,41</sup> The truncation energy of the plane-wave basis set is set to 400 eV. The convergence criteria for structural optimization are that the change in electron energy must be less than  $1 \times 10^{-7}$  eV and the force change must be less than 0.01 eV Å<sup>-1</sup>. Monkhorst–Pack sampling is performed in the Brillouin zone using a  $3 \times 3 \times 1$  k-point grid. For the transition state search of the primitive reaction, the climbing-image nudged elastic band (CI-NEB) method was employed to identify the transition-state structure.<sup>42,43</sup> Subsequently, the dimer method is employed to optimize the system, thereby obtaining the transition state structure of the elementary reaction. Finally, frequency analysis is performed on the optimized transition state, and the presence of a single imaginary frequency is used as the criterion to verify the correctness of the transition state structure. The convergence criteria for the transition state energy and force are set to  $1 \times 10^{-7}$  eV and 0.03 eV Å<sup>-1</sup>, respectively.<sup>44,45</sup>

The Pd(111) surface is modeled using a P( $4 \times 4$ ) periodic supercell consisting of 4 atomic layers. According to experimental findings, the Ni/Pd(111)-O model is constructed by substituting a Pd atom in the topmost layer of the Pd(111) surface with a Ni atom and positioning an O atom on the surface. LA contains an abundance of  $-\text{NH}_2$  functional groups. Therefore, to construct the Ni/Pd(111)-O

model after LA modification, we introduced an  $-\text{NH}_2$  group onto the surface of Ni/Pd(111)-O, naming this modified structure Ni/Pd(111)-ON. We performed structural optimization on the Ni/Pd(111)-O and Ni/Pd(111)-ON models, and the optimized structures were utilized for subsequent calculations. A vacuum layer with a thickness of at least 15 Å was introduced to prevent correlation effects between distinct surface models. To accurately describe the bulk phase properties of the Pd(111), Ni/Pd(111)-O, and Ni/Pd(111)-ON surfaces under reaction conditions, calculations were performed with the bottom two atomic layers fixed, while allowing relaxation of the remaining atoms and any adsorbed species.

The activation energy  $E_a$  and reaction energy  $\Delta E$  of the elementary reaction are calculated using the following equation:

$$E_a = E_{TS} - E_{IS} \quad (5)$$

$$\Delta E = E_{FS} - E_{IS} \quad (6)$$

$E_{IS}$ ,  $E_{FS}$ , and  $E_{TS}$  represent the initial state, final state, and transition state of the elementary reaction, respectively.

The adsorption energy for M species ( $E_{ads}(M)$ ) is calculated using the following equation:

$$E_{ads}(M) = E_{M-surface} - E_{surface} - E_M \quad (7)$$

$E_{M-surface}$ ,  $E_{surface}$  and  $E_M$  represent the total energy of the adsorbed species on the surface, the energy of the clean surface, and the energy of the adsorbed species in the gas phase, respectively. Therefore, a

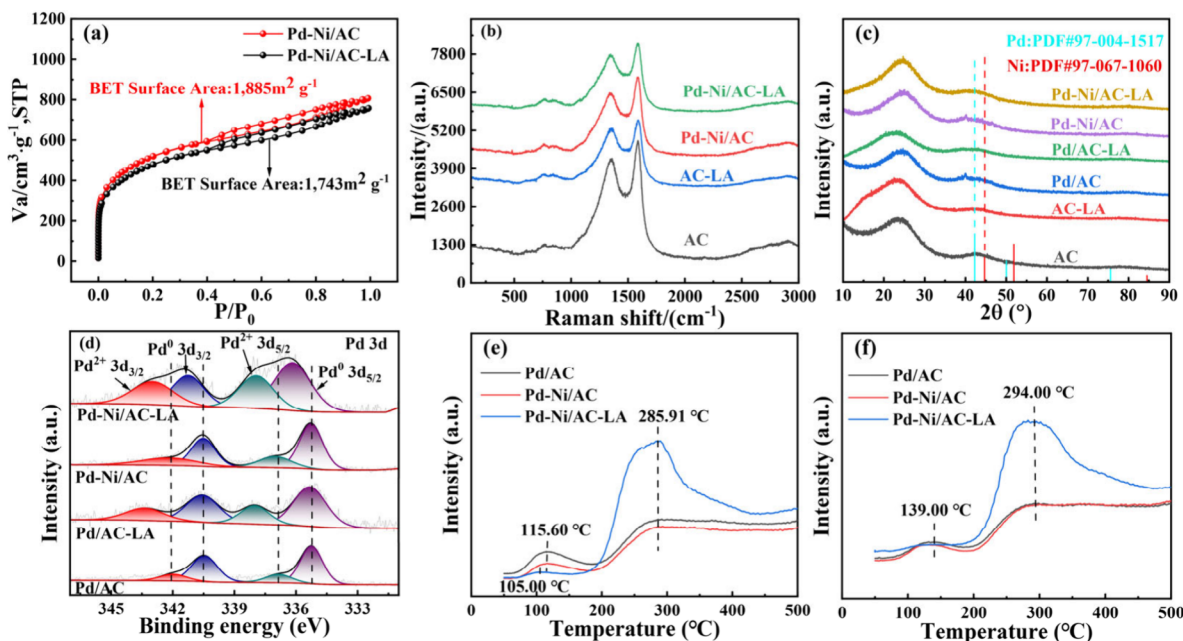


**Figure 4.** (a)  $N_2$  adsorption and desorption isothermal adsorption lines of Pd-Ni/AC and Pd-Ni/AC-LA catalysts. (b) Raman spectra of AC, AC-LA, Pd-Ni/AC, and Pd-Ni/AC-LA. (c) XRD spectra of AC, AC-LA, Pd/AC, Pd/AC-LA, Pd-Ni/AC, and Pd-Ni/AC-LA. (d) XPS high-resolution spectra of Pd 3d for Pd/AC, Pd/AC-LA, Pd-Ni/AC, and Pd-Ni/AC-LA. (e)  $H_2$ -TPD spectra of Pd/AC, Pd-Ni/AC, and Pd-Ni/AC-LA catalysts. (f)  $O_2$ -TPD spectra of Pd/AC, Pd-Ni/AC, and Pd-Ni/AC-LA catalysts.

more negative  $E_{ads}(M)$  value indicates stronger adsorption of the corresponding species M on the surface. The calculation of activation energy ( $E_a$ ), reaction energy ( $\Delta E$ ), and adsorption energy ( $E_{ads}$ ) all incorporate corrections for zero-point energy (ZPE).

## RESULTS AND DISCUSSION

**Catalyst Characterization.** To confirm the successful functionalization of the Pd–Ni catalyst by LA, transmission electron microscopy (TEM) was employed to examine the morphology, size, dispersion, and composition of the catalyst. As illustrated in Figure 3(a) and (b), metal particles on the Pd-Ni/AC-LA catalyst exhibit excellent dispersion with an average particle size of 4.16 nm. This is notably smaller than the average particle sizes observed for Pd/AC (5.17 nm, Figure S1(a) and (a')), Pd/AC-LA (4.94 nm, Figure S1(b) and (b')), and Pd-Ni/AC (5.31 nm, Figure S1(c) and (c')) catalysts. These findings suggest that LA-functionalization enhances the dispersion of metal particles and effectively reduces their size. It has been demonstrated that a narrow particle size distribution and smaller particle sizes are advantageous for the synthesis of  $H_2O_2$  from  $H_2$  and  $O_2$  under ambient conditions.<sup>46,47</sup> High-resolution TEM (HRTEM) images of the metal particles are presented in Figure 3(c) and 3(d-f). These images reveal that the Pd nanoparticles on the surface of the prepared catalyst are predominantly composed of Pd(111) crystal planes. Tian et al. demonstrated that the Pd(111) crystal plane serves as the primary active site for the direct synthesis of  $H_2O_2$  from  $H_2$  and  $O_2$ .<sup>48</sup> By quantitatively measuring the crystal lattice spacing of Pd(111) facets on different catalysts, we found that the lattice parameter of Pd(111) facets for Pd-Ni/AC-LA is 0.2064 nm, which is significantly lower than that of Pd-Ni/AC (0.2171 nm). This indicates that LA-functionalization effectively reduces the interplanar spacing of Pd(111), thereby enhancing the selectivity toward  $H_2O_2$  production. Figure 3(d-j) displays the energy dispersive X-ray spectrum (EDS) of Pd-Ni/AC-LA.

The presence of abundant and highly dispersed nitrogen signals in the spectra suggests that LA has successfully functionalized the Pd-Ni/AC-LA composite. Simultaneously, it is evident that Pd and Ni are highly uniformly dispersed within the carbon support. The signal intensity of Ni is observed to be weaker than that of Pd, which correlates well with the elemental concentrations determined by ICP analysis. Furthermore, the overlapping signals of Pd and Ni suggest the formation of a Pd–Ni alloy. The distribution patterns of Pd and Ni shown in Figure 3(k) and (l) are remarkably similar, providing further evidence that Pd and Ni have formed Pd–Ni alloys.

To elucidate the functionalization of Pd-Ni/AC-LA with LA, the catalysts were characterized using BET, XPS, FT-IR, Raman spectroscopy, and TPD. As illustrated in Figure 4(a), the specific surface area of Pd-Ni/AC-LA is  $1743\text{ m}^2\text{ g}^{-1}$ , and the pore volume is  $1.17\text{ cm}^3\text{ g}^{-1}$ . These values are marginally lower than those of Pd-Ni/AC, which has a specific surface area of  $1885\text{ m}^2\text{ g}^{-1}$  and a pore volume of  $1.25\text{ cm}^3\text{ g}^{-1}$ . This suggests that LA functionalization has a minimal impact on the pore structure of the catalyst and support. As illustrated in Figure S2(a) and (b), the characteristic peaks of the C 1s XPS spectra for Pd-Ni/AC and Pd-Ni/AC-LA at 284.04 and 285.64 eV are attributed to C–C and C=C bonds, respectively.<sup>49,50</sup> The O 1s XPS spectra of Pd-Ni/AC and Pd-Ni/AC-LA (Figure S3(a), (b)) exhibit three characteristic peaks at 531.04, 532.09, and 534.96 eV, corresponding to C=O, –C–O–O, and –C–O bonds, respectively.<sup>51</sup> The characteristic peak intensities and binding energies of C 1s and O 1s for Pd-Ni/AC and Pd-Ni/AC-LA are comparable, suggesting that LA-functionalization has minimal impact on the AC support itself. The N 1s XPS spectrum of Pd-Ni/AC-LA, as shown in Figure S4(a), exhibits characteristic peaks at 398.52, 399.64, and 400.98 eV, which are attributed to the –C=N, –C–N, and –N–C=O bonds, respectively.<sup>51</sup> The results demonstrate that LA has successfully functionalized AC through chemical

bonding. Figure S5(a) and (b) display the infrared spectra of AC and Pd-Ni/AC-LA. The characteristic peak at  $3068\text{ cm}^{-1}$  is assigned to the stretching vibration of  $-\text{NH}_3^+$ , while the peak at  $1405\text{ cm}^{-1}$  corresponds to the bending vibration of  $-\text{COO}^-$ .<sup>52</sup> The peak strength of Pd-Ni/AC-LA is lower than that of AC, suggesting the formation of intermolecular hydrogen bonds. The stretching vibration of  $-\text{COOH}$  at  $1733\text{ cm}^{-1}$  and the stretching vibration of  $-\text{C}=\text{N}$  at  $1653\text{ cm}^{-1}$  (for Pd-Ni/AC-LA) shifted to  $1691\text{ cm}^{-1}$  and  $1609\text{ cm}^{-1}$ , respectively. This shift further confirms the formation of hydrogen bonds.<sup>53,54</sup> The presence of amide characteristic peaks at  $1386$ ,  $1609$ , and  $3422\text{ cm}^{-1}$ , as well as the  $-\text{N}-\text{C}=\text{O}$  bond observed at  $400.98\text{ eV}$  in the N 1s XPS spectrum of Pd-Ni/AC-LA, indicates the formation of covalent bonds between LA and AC.<sup>52,55</sup> As illustrated in Figure 4(b), the  $I_{\text{D}}/I_{\text{G}}$  ratios of the D band at  $1345.94\text{ cm}^{-1}$  and the G band at  $1586.27\text{ cm}^{-1}$  in the Raman spectra remained constant, indicating that LA-functionalization does not induce structural damage to AC.<sup>56</sup> In addition, studies have shown that LA and AC can also bind through noncovalent interactions, including hydrophobic and cation- $\pi$  interactions, analogous to the binding mechanism between poly-L-lysine and carbon nanotubes.<sup>57</sup> Based on the aforementioned characterization results, it is evident that LA effectively functionalizes AC via both covalent bonds (specifically amide bonds) and noncovalent interactions (including hydrogen bonding, hydrophobic effects, and cation- $\pi$  interactions).<sup>31</sup>

XRD patterns of all catalysts are presented in Figure 4(c). Notably, each sample exhibits a distinctive diffraction peak at  $23.0^\circ$ , corresponding to the characteristic diffraction peak of the C(002) crystal plane of AC.<sup>58</sup> Notably, for the 1.0% Pd and 0.1% Ni catalysts (Pd-Ni/AC-LA), no distinct diffraction peaks corresponding to Pd or Pd-Ni nanoparticles were observed. It is evident that when the Pd loading is reduced to 1.0%, the diffraction signal becomes weak, possibly due to the low concentrations of Pd and Ni as well as a poor signal-to-noise ratio, making detection by the instrument challenging.

The XPS spectra and quantitative analysis of Pd 3d for all catalysts are presented in Figure 4(d) and Table 1. The peaks

from 0.28 (Pd/AC) to 0.76 (Pd-Ni/AC-LA), an increase of 63.16%. The characteristic peaks of  $\text{Pd}^0$  and  $\text{Pd}^{2+}$  shift to higher binding energies (+0.93 eV), and the ratio of  $\text{Pd}^{2+}/\text{Pd}^0$ , as well as the extent of this shift, is greater than that observed for Pd/AC-LA and Pd-Ni/AC. According to Lee and Chen et al., increasing the  $\text{Pd}^{2+}$  content can reduce the dissociation of the O–O bond, thereby mitigating adverse side reactions.<sup>71–74</sup> The enhanced interaction between Pd and Ni, as well as the interaction between Pd and AC-LA, leads to an increased  $\text{Pd}^{2+}/\text{Pd}^0$  ratio and a shift toward higher binding energy.

The  $\text{H}_2$ -TPD characterization results of the catalyst are presented in Figure 4(e). The desorption peaks at  $105.11$  and  $115.60\text{ }^\circ\text{C}$  are attributed to molecular  $\text{H}_2$  desorption, while the desorption peak at  $285.91\text{ }^\circ\text{C}$  is associated with atomic H desorbed from the Pd–H species.<sup>75</sup> The H atom desorption from Pd-Ni/AC-LA is the highest among all samples, indicating that Pd-Ni/AC-LA exhibits the strongest capability for adsorption and dissociation of  $\text{H}_2$  molecules. The  $\text{O}_2$ -TPD characterization results of the catalyst are presented in Figure 4(f), the desorption peak at  $139\text{ }^\circ\text{C}$  is attributed to the desorption of weakly adsorbed  $\text{O}_2$  molecules on Pd, while the desorption peak at  $294.00\text{ }^\circ\text{C}$  corresponds to the desorption of O atoms formed by the dissociation of  $\text{O}_2$  on Pd.<sup>76,77</sup> It is noteworthy that Pd-Ni/AC-LA exhibits the highest level of O atom desorption. This observation appears contradictory to the XPS characterization results, which indicate a high  $\text{Pd}^{2+}$  content. Typically,  $\text{Pd}^{2+}$  effectively inhibits O–O bond dissociation. The discrepancy may be attributed to the decomposition of O atoms by LA at elevated temperatures.

The influence of Ni doping on  $\text{H}_2\text{O}_2$  yield was investigated by varying the molar amounts of Ni. As illustrated in Figure 5(a), a volcano-like relationship exists between  $\text{H}_2\text{O}_2$  yield and the Ni/Pd ratio. When the Ni/Pd ratio is 0.1, the yield and concentration of the Pd-Ni/AC catalyst reach their highest values, at  $298.80\text{ g kg}_{\text{cat}}^{-1}\text{ h}^{-1}$  and 2.11 wt %, respectively. When the Ni doping level is low, its ability to modulate the electronic properties of Pd is limited, resulting in an insufficient change in the electronic structure of Pd. As the amount of Ni added increases, its capability to modulate the electronic structure of Pd is enhanced, thereby promoting a more significant increase in  $\text{H}_2\text{O}_2$  production and concentration. However, as the Ni content increases further, a portion of Ni deposits on the surface of Pd nanoparticles, hindering the reactants ( $\text{H}_2$  and  $\text{O}_2$ ) from accessing the active sites. This leads to a reduction in both the production rate and concentration of  $\text{H}_2\text{O}_2$ .<sup>24</sup> As illustrated in Figure 5(b), a volcano-like relationship exists between  $\text{H}_2\text{O}_2$  yield and LA dosage. In conjunction with BET characterization (Figure 4(a)) and Table 1, an excessive amount of LA can occupy the pore volume of carbon carriers, thereby hindering the contact between  $\text{H}_2$  and  $\text{O}_2$  with the Pd active sites. Conversely, insufficient LA addition results in inadequate electronic modulation of Pd. The findings indicate that the optimal LA dosage is 10 mg. The results of Ni doping and LA-functionalization demonstrated that appropriate levels of Ni doping and LA-functionalization could significantly enhance the yield of  $\text{H}_2\text{O}_2$ . The  $\text{H}_2\text{O}_2$  yield and concentration achieved by the Pd-Ni/AC-LA catalyst are  $574.31\text{ g kg}_{\text{cat}}^{-1}\text{ h}^{-1}$  and 4.05 wt %, respectively, outperforming many previously reported catalysts as shown in Table 2. Based on these experimental findings, we successfully synthesized the Pd-Ni/AC-LA catalyst coregulated by Ni and LA under optimal conditions of Ni/Pd = 0.1 and LA = 10 mg. As depicted in Figure 5(c), the TOF of

**Table 1. Quantitative Analysis Results of Pd 3d XPS Spectra for Pd/AC, Pd/AC-LA, Pd-Ni/AC, and Pd-Ni/AC-LA**

Catalysts	Pd Species	3d <sub>5/2</sub>		$\text{Pd}^{2+}/\text{Pd}^0$
		Peak BE (eV)	Peak BE (eV)	
Pd/AC	Pd <sup>0</sup>	335.24	340.46	0.28
	Pd <sup>2+</sup>	336.84	341.97	
Pd/AC-LA	Pd <sup>0</sup>	335.25	340.48	0.41
	Pd <sup>2+</sup>	337.01	342.21	
Pd-Ni/AC	Pd <sup>0</sup>	335.27	340.51	0.45
	Pd <sup>2+</sup>	337.01	342.17	
Pd-Ni/AC-LA	Pd <sup>0</sup>	336.17	341.25	0.76
	Pd <sup>2+</sup>	337.93	342.98	

at  $335.24$  and  $340.46\text{ eV}$  are assigned to the  $\text{Pd}^0$  3d<sub>5/2</sub> and  $\text{Pd}^0$  3d<sub>3/2</sub> states, respectively.<sup>59,60</sup> Compared to Pd/AC, the higher binding energy in Pd-Ni/AC-LA can primarily be attributed to the initial state effect and the final state effect of the nuclear hole, which are induced by electron transfer to O and  $-\text{NH}_2$ .<sup>61–69</sup>

The peaks at  $336.84$  and  $341.97\text{ eV}$  are identified as the characteristic peaks corresponding to  $\text{Pd}^{2+}$  3d<sub>5/2</sub> and  $\text{Pd}^{2+}$  3d<sub>3/2</sub>, respectively.<sup>65,70</sup> The proportion of  $\text{Pd}^{2+}/\text{Pd}^0$  increased

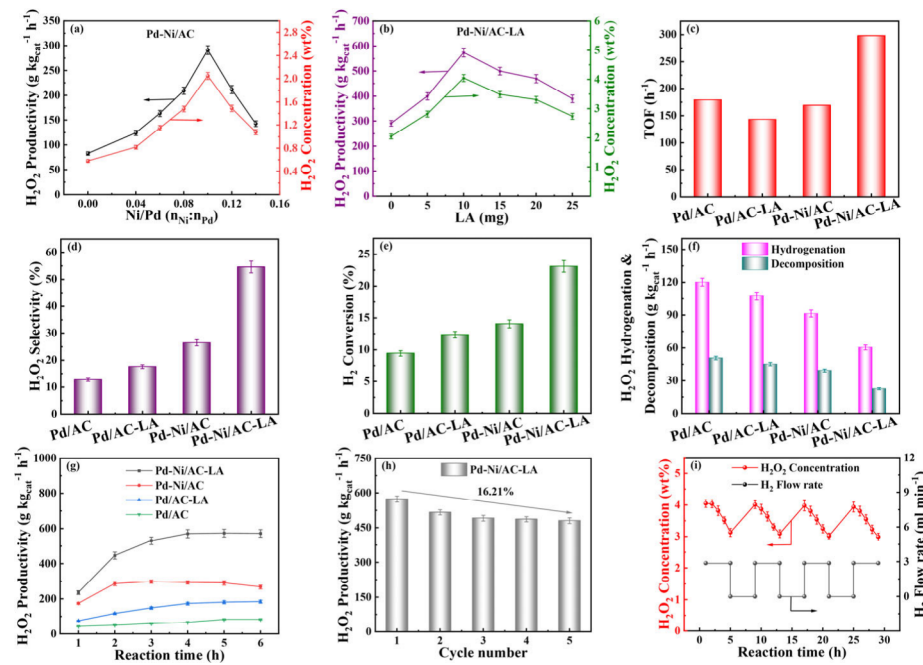


**Figure 5.** (a) Yield and concentration of  $\text{H}_2\text{O}_2$  synthesized over Pd-Ni/AC catalysts with different Ni: Pd. (b) Yield and concentration of  $\text{H}_2\text{O}_2$  synthesized by Pd-Ni/AC-LA catalysts with different LA additions. (c) Turnover rate (TOF) of Pd/AC, Pd/AC-LA, Pd-Ni/AC and Pd-Ni/AC-LA catalysts. (d) Selectivity of  $\text{H}_2\text{O}_2$  by Pd/AC, Pd/AC-LA, Pd-Ni/AC and Pd-Ni/AC-LA. (e) Conversion of  $\text{H}_2$  for Pd/AC, Pd/AC-LA, Pd-Ni/AC and Pd-Ni/AC-LA. (f) Hydrogenation and decomposition of  $\text{H}_2\text{O}_2$  of Pd/AC, Pd/AC-LA, Pd-Ni/AC and Pd-Ni/AC-LA. (g) Effect of reaction time on the yield of  $\text{H}_2\text{O}_2$  synthesized by Pd/AC, Pd/AC-LA, Pd-Ni/AC and Pd-Ni/AC-LA. (h)  $\text{H}_2\text{O}_2$  yield of Pd-Ni/AC-LA in cycling experiments. (i) Pd-Ni/AC-LA catalysts for DSHP recovery and recirculation on a microreactor.

**Table 2. Comparison of DSHP Performance between Pd-Ni/AC-LA and Existing Catalysts**

Reactor type	Catalyst	T (K)	P (bar)	Solvent	Productivity ( $\text{g kg}_{\text{cat}}^{-1} \text{h}^{-1}$ )	Reference
continuous	Pd <sub>1</sub> Au <sub>0.7</sub> /TiO <sub>2</sub>	296	10	$\text{H}_2\text{O} + \text{acid} + \text{NaBr}$	12.24	Inoue <sup>34</sup>
continuous	Pd/Al <sub>2</sub> O <sub>3</sub>	298	1	MeOH + $\text{H}_2\text{O} + \text{acid} + \text{NaBr}$	29.10	Yang <sup>36</sup>
continuous	Pd-Sn/Al <sub>2</sub> O <sub>3</sub>	298	1	MeOH + $\text{H}_2\text{O} + \text{acid} + \text{NaBr}$	31.24	Yang <sup>78</sup>
microreactor	5% Pd/various	293	10	$\text{H}_2\text{O} + \text{acid} + \text{Br}$	264.58	Inoue <sup>33</sup>
microreactor	1%Au-Pd/TiO <sub>2</sub>	275	10	66%MeOH + 34% $\text{H}_2\text{O}$	117.59	Simon <sup>79</sup>
trickle bed reactor	2.5%Pd/CeO <sub>2</sub> , ZrO <sub>2</sub>	263	10	MeOH	11.76–14.70	Biasi <sup>80</sup>
trickle bed reactor	2.5%AuPd/CeO <sub>2</sub> , ZrO <sub>2</sub>	263	10	MeOH	up to 52.91	Biasi <sup>81</sup>
continuous	Pd-Ni/AC	298	1	MeOH + acid + NaBr	298.80	This work
continuous	Pd-Ni/AC-LA	298	1	MeOH + acid + NaBr	574.31	This work

Pd-Ni/AC-LA is 298, outperforming Pd/AC, Pd/AC-LA, and Pd-Ni/AC catalysts.

Figure 5(d) and (e) present the comparative evaluation results of  $\text{H}_2\text{O}_2$  selectivity and  $\text{H}_2$  conversion for various catalysts. The Pd-Ni/AC-LA catalyst exhibited superior catalytic performance, demonstrating significantly higher  $\text{H}_2\text{O}_2$  selectivity and  $\text{H}_2$  conversion compared to other analogous catalysts. The superior catalytic performance of Pd-Ni/AC-LA is likely attributed to the surface electronic state and particle size of Pd. As shown in Table 1, the  $\text{Pd}^{2+}/\text{Pd}^0$  ratio of the Pd-Ni/AC-LA catalyst, which benefits from the synergistic effect of Ni and LA, reaches 0.76. This elevated  $\text{Pd}^{2+}/\text{Pd}^0$  ratio effectively suppresses the dissociation of the O–O bond, thereby enhancing the selectivity of  $\text{H}_2\text{O}_2$ . Based on the TEM analysis of the metal particle distribution, it is evident that Pd-Ni/AC-LA exhibits the smallest average particle size of Pd nanoparticles. The reduced particle size facilitates enhanced  $\text{H}_2$  conversion efficiency.<sup>46</sup>

Hydrogenation (under  $\text{H}_2$  atmosphere) and decomposition (under  $\text{N}_2$  atmosphere) experiments were conducted to

investigate the side reactions of hydrogenation and decomposition on the catalyst. As illustrated in Figure 5(f), the Pd-Ni/AC-LA catalyst exhibited the lowest rates of hydrogenation and decomposition, suggesting that the dual modification through Ni doping and LA-functionalization effectively minimized the hydrogenation and decomposition rates of  $\text{H}_2\text{O}_2$ . The impact of reaction time on  $\text{H}_2\text{O}_2$  yield was systematically investigated. As illustrated in Figure 5(g), the yield of  $\text{H}_2\text{O}_2$  for all catalysts progressively increased with extended reaction time before reaching a plateau. Notably, the Pd-Ni/AC-LA catalyst exhibited the highest  $\text{H}_2\text{O}_2$  yield. The results demonstrate that Ni doping and LA-functionalization are essential for the dual modification. Utilizing a microreactor can effectively minimize the contact time between  $\text{H}_2\text{O}_2$  and the catalyst, thereby reducing the decomposition of  $\text{H}_2\text{O}_2$ . After five cycles of experiments, the Pd-Ni/AC-LA catalyst maintains high activity, as illustrated in Figure 5(h). This suggests that the dual modification through Ni doping and LA-functionalization significantly enhances both the stability and regenerability of the catalyst.

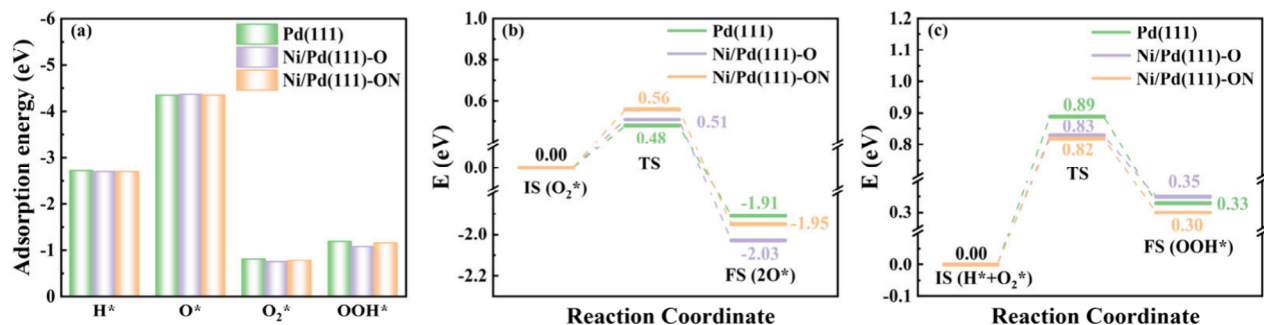


**Figure 6.** (a) Adsorption energies of  $\text{H}^*$ ,  $\text{O}^*$ ,  $\text{O}_2^*$ , and  $\text{OOH}^*$  on  $\text{Pd}(111)$ ,  $\text{Ni}/\text{Pd}(111)\text{-O}$ , and  $\text{Ni}/\text{Pd}(111)\text{-ON}$  surfaces. (b) The activation energy for  $\text{O}_2^*$  dissociation on the  $\text{Pd}(111)$ ,  $\text{Ni}/\text{Pd}(111)\text{-O}$ , and  $\text{Ni}/\text{Pd}(111)\text{-ON}$  surfaces. (c) The activation energy for the hydrogenation of  $\text{O}_2^*$  on  $\text{Pd}(111)$ ,  $\text{Ni}/\text{Pd}(111)\text{-O}$ , and  $\text{Ni}/\text{Pd}(111)\text{-ON}$  surfaces.

Excessive adsorption of  $\text{H}_2$  during catalyst use leads to  $\text{H}_2$  poisoning on the catalyst surface, thereby reducing its activity.<sup>78</sup> As illustrated in Figure 5(i), when  $\text{H}_2$  is intermittently injected while  $\text{O}_2$  is continuously supplied, the catalyst's activity is partially restored after  $\text{O}_2$  consumes the  $\text{H}_2$  adsorbed at the Pd active sites. The results demonstrated that the intermittent introduction of  $\text{H}_2$  partially restored the catalyst activity. This demonstrates that the catalyst can be effectively reactivated through intermittent  $\text{H}_2$  supply in the microreactor. The simplicity of this process allows for multiple online reactiverations, significantly reducing operational costs.

**DFT Calculation.** The XRD, TEM, and XPS results indicate that the synthesized Pd nanoparticles predominantly exhibit the  $\text{Pd}(111)$  crystal plane. Additionally, Ni atoms have been successfully doped onto the surface of the Pd nanoparticles, which in turn affects the chemical state of Pd through electronic interactions. FT-IR analysis confirmed that LA successfully adhered to the AC of Pd nanoparticles loaded with Ni, thereby altering the chemical state of Pd. Based on the experimental results, we constructed three distinct surface structures:  $\text{Pd}(111)$ ,  $\text{Ni}/\text{Pd}(111)\text{-O}$ , and  $\text{Ni}/\text{Pd}(111)\text{-ON}$ , to simulate undoped Pd nanoparticles, Ni-doped Pd nanoparticles, and LA-modified Ni-doped Pd nanoparticles, respectively, as illustrated in Figure S6.

In order to verify the accuracy of the model, we first analyzed the charge distribution of each element of the three models through bader charge, and the results are shown in Figure S7. The analysis results indicate that the Pd atoms in the  $\text{Pd}(111)$ ,  $\text{Ni}/\text{Pd}(111)\text{-O}$ , and  $\text{Ni}/\text{Pd}(111)\text{-ON}$  models possess positive charges of 0.00, 0.23, and 0.41 e, respectively. This finding is in agreement with the XPS characterization results, thereby validating the accuracy of the models. The electronegativity of Pd is higher than that of Ni. (Pauling electronegativity scale Ni: 1.91, Pd: 2.20).<sup>82–85</sup> When Ni is doped on the surface of Pd, the electronegativity difference between the two elements facilitates electron transfer from Ni to Pd. However, due to its higher reactivity, Ni tends to interact with  $\text{O}_2$  in the ambient environment, leading to oxygen adsorption on the surface of Ni-doped Pd(111). The electronegativity of O is up to 3.44.<sup>86</sup> When adsorbed on the surface of Ni-doped Pd, it facilitates the transfer of electrons from Ni and Pd atoms to O atoms, leading to an electron-deficient state in the Pd and Ni atoms. The  $-\text{NH}_2$  functional group exhibits strong electronegativity. Upon adsorption on the surface of Pd nanoparticles, it facilitates electron transfer from Pd to the N element, leading to an electron-deficient state in the Pd nanoparticles. Under the synergistic effect of the O

and  $-\text{NH}_2$  functional groups, the positive charge on the Pd element in the  $\text{Ni}/\text{Pd}(111)\text{-ON}$  model is further enhanced, which facilitates maintaining the electron-deficient state of the Pd nanoparticles. In conjunction with the DFT simulation results, we can gain a deeper understanding of the reasons for the shift of the Pd  $3\text{d}_{3/2}$  peak binding energy toward higher energy levels in the XPS analysis of Pd-Ni/AC and Pd-Ni/AC-LA samples. Ni doping facilitates the coverage of Pd surfaces by oxygen. Oxygen adsorbs on the surface of Pd nanoparticles, transferring electrons from Pd and Ni to O, which results in a shift of the Pd  $3\text{d}_{3/2}$  binding energy peak to higher energy levels. When synthesizing the LA-functionalized Pd-Ni/AC-LA catalyst, the abundant  $-\text{NH}_2$  functional groups of LA further enhanced electron transfer, thereby promoting the  $\text{Pd}^0$   $3\text{d}_{3/2}$  peak binding energy to shift to a higher energy level.

The adsorption energies of key intermediates, including  $\text{H}$ ,  $\text{O}$ ,  $\text{O}_2$ , and  $\text{OOH}$ , on  $\text{Pd}(111)$ ,  $\text{Ni}/\text{Pd}(111)\text{-O}$ , and  $\text{Ni}/\text{Pd}(111)\text{-ON}$  surfaces were calculated. As illustrated in Figure 6, the adsorption energies of  $\text{H}$ ,  $\text{O}$ ,  $\text{O}_2$ , and  $\text{OOH}$  species on the  $\text{Pd}(111)$  surface are  $-2.71$  eV,  $-4.35$  eV,  $-0.81$  eV, and  $-1.18$  eV, respectively. Notably, the adsorption energies of  $\text{H}$ ,  $\text{O}_2$ , and  $\text{OOH}$  on the  $\text{Pd}(111)$  surface are more negative (i.e., stronger) compared to those on  $\text{Ni}/\text{Pd}(111)\text{-O}$  and  $\text{Ni}/\text{Pd}(111)\text{-ON}$  surfaces. This suggests that both  $\text{Ni}/\text{Pd}(111)\text{-O}$  and  $\text{Ni}/\text{Pd}(111)\text{-ON}$  partially inhibit the adsorption of  $\text{H}$ ,  $\text{O}_2$ , and  $\text{OOH}$  on the Pd surface.

Thermodynamically,  $\text{H}_2$  and  $\text{O}_2$  can directly synthesize both  $\text{H}_2\text{O}_2$  and  $\text{H}_2\text{O}$ .<sup>87</sup>  $\text{O}_2^*$  ( $^*$  denotes the adsorbed state) and  $\text{OOH}^*$  are crucial intermediates in the direct synthesis of  $\text{H}_2\text{O}_2$  from  $\text{H}_2$  and  $\text{O}_2$ , and the activation levels of these intermediates directly influence the formation of  $\text{H}_2\text{O}_2$ . As illustrated in Figure 6(a), the adsorption energies of O atoms on  $\text{Pd}(111)$ ,  $\text{Ni}/\text{Pd}(111)\text{-O}$ , and  $\text{Ni}/\text{Pd}(111)\text{-ON}$  surfaces are  $-4.35$  eV,  $-4.37$  eV, and  $-4.35$  eV, respectively. These values suggest that all three surfaces exhibit strong adsorption capacities for O atoms, with  $\text{Ni}/\text{Pd}(111)\text{-O}$  showing slightly stronger binding. The adsorption energies of  $\text{O}_2$  on  $\text{Pd}(111)$ ,  $\text{Ni}/\text{Pd}(111)\text{-O}$ , and  $\text{Ni}/\text{Pd}(111)\text{-ON}$  surfaces are  $-0.81$  eV,  $-0.74$  eV, and  $-0.78$  eV, respectively. The relatively lower adsorption energies on the  $\text{Ni}/\text{Pd}(111)\text{-O}$  and  $\text{Ni}/\text{Pd}(111)\text{-ON}$  surfaces reduce the likelihood of excessive  $\text{O}_2$  adsorption. After adsorption, the O–O bond lengths on the surfaces of  $\text{Pd}(111)$ ,  $\text{Ni}/\text{Pd}(111)\text{-O}$ , and  $\text{Ni}/\text{Pd}(111)\text{-ON}$  are  $1.373$  Å,  $1.329$  Å, and  $1.337$  Å, respectively, all of which are longer than that of gaseous oxygen ( $1.24$  Å). This indicates that  $\text{O}_2$  adsorbed on  $\text{Pd}(111)$ ,  $\text{Ni}/\text{Pd}(111)\text{-O}$ , and  $\text{Ni}/\text{Pd}(111)\text{-ON}$

surfaces is fully activated, with the activation degree following the trend: Pd(111) > Ni/Pd(111)-ON > Ni/Pd(111)-O.

The hydrogenation and dehydrogenation of the O–O bond in the direct synthesis of H<sub>2</sub>O<sub>2</sub> from H<sub>2</sub> and O<sub>2</sub> is a competitive side reaction that significantly impacts the formation of H<sub>2</sub>O<sub>2</sub>. To enhance the catalytic performance in the direct synthesis of H<sub>2</sub>O<sub>2</sub> from H<sub>2</sub> and O<sub>2</sub>, it is necessary to reduce the activation energy barrier for O–O bond cleavage while increasing the activation energy for dissociation. Therefore, we initially determined the dissociation energy and energy barrier of O<sub>2</sub>\* with the results presented in Figure 6(b). The surface dissociation energies of O<sub>2</sub>\* on Pd(111), Ni/Pd(111)-O, and Ni/Pd(111)-ON are −1.91 eV, −2.03 eV, and −1.95 eV, respectively. These relatively high dissociation energies suggest that it is unlikely for O<sub>2</sub> to recombine into molecular O<sub>2</sub> after dissociation on the Pd surface. The primary product of the dissociated O\* atom is H<sub>2</sub>O; therefore, inhibiting the dissociation of O<sub>2</sub> on the Pd surface constitutes the first crucial step in the direct synthesis of H<sub>2</sub>O<sub>2</sub> from H<sub>2</sub> and O<sub>2</sub>. The dissociation energy barriers of O<sub>2</sub>\* on Pd(111), Ni/Pd(111)-O, and Ni/Pd(111)-ON surfaces are 0.48, 0.51, and 0.56 eV, respectively. The higher dissociation energy barriers on Ni/Pd(111)-O and Ni/Pd(111)-ON surfaces indicate that the dissociation of O<sub>2</sub>\* is less favorable on these surfaces, which is beneficial for the direct synthesis of H<sub>2</sub>O<sub>2</sub>. We subsequently determined the activation energy and energy barrier for the O<sub>2</sub>\* hydroactivation process. The results are presented in Figure 6(c). Specifically, the activation energies for the formation of OOH\* via O<sub>2</sub>\* hydrogenation on Pd(111), Ni/Pd(111)-O, and Ni/Pd(111)-ON surfaces were found to be 0.33, 0.35, and 0.30 eV, respectively. Correspondingly, the activation energy barriers were measured at 0.88, 0.83, and 0.82 eV, respectively. Compared to Pd(111), the Ni/Pd(111)-O and Ni/Pd(111)-ON surfaces exhibit lower activation energy barriers, making them more conducive to OOH\* generation.

Based on the experimental and theoretical findings, we can gain a comprehensive understanding of the mechanisms by which Ni doping and LA-functionalization influence catalytic activity. Ni doping and LA modification facilitate the transfer of electrons from Pd to O and N, resulting in an electron-deficient state for Pd. This reduces the activation energies for O<sub>2</sub>\* and OOH\* on Ni/Pd(111)-O and Ni/Pd(111)-ON surfaces while increasing the activation energies for their dissociation reactions. Consequently, this promotes the improvement of H<sub>2</sub>O<sub>2</sub> selectivity and yield. Therefore, in the catalyst activity test, the Ni-doped and LA-functionalized Pd-based catalysts exhibited superior catalytic performance.

## CONCLUSION

In this study, we successfully synthesized Ni-doped and LA-functionalized Pd-Ni/AC-LA catalysts, which exhibited remarkable DSHP catalytic activity in microreactors. H<sub>2</sub>O<sub>2</sub> production and concentration reached 574.31 g kg<sub>cat</sub><sup>−1</sup> h<sup>−1</sup> and 4.05 wt %, respectively. Notably, the activity was maintained at 481.01 g kg<sub>cat</sub><sup>−1</sup> h<sup>−1</sup> even after 5 cycles. TEM characterization revealed that LA-functionalization significantly enhanced the dispersion of Pd nanoparticles on the surface of the Pd-Ni/AC-LA catalyst. FT-IR analysis confirms that LA effectively functionalizes AC via both covalent and noncovalent interactions. XPS analysis revealed that the comodification of Pd with Ni and LA resulted in a significant electron-deficient state, with a Pd<sup>2+</sup>/Pd<sup>0</sup> ratio as high as 0.76. DFT results

indicate that Ni doping and LA-functionalization facilitate electron transfer from Pd to O and N, thereby placing Pd in an electron-deficient state. This effect reduces the activation energy for the hydrogenation of O<sub>2</sub>\* and OOH\*, while simultaneously increasing the activation energy for the dissociation reaction, ultimately enhancing the selectivity and yield of H<sub>2</sub>O<sub>2</sub>. O<sub>2</sub>-TPD analysis revealed that the results were underestimated by DFT analysis, and higher Pd<sup>2+</sup> concentrations significantly inhibited the O–O bond dissociation of O<sub>2</sub>. The results of this study demonstrate the feasibility of Ni-doped and LA-functionalized Pd-Ni/AC-LA catalysts for synthesizing high-concentration H<sub>2</sub>O<sub>2</sub> in a microreactor.

## ASSOCIATED CONTENT

### Supporting Information

The Supporting Information is available free of charge at <https://pubs.acs.org/doi/10.1021/acs.langmuir.Sc00997>.

TEM images of Pd/AC, Pd/AC-LA, and Pd-Ni/AC catalysts, along with their particle size distributions and corresponding HRTEM images. The C 1s XPS spectra of Pd-Ni/AC and Pd-Ni/AC-LA catalysts. The O 1s XPS spectra of Pd-Ni/AC and Pd-Ni/AC-LA catalysts. The N 1s XPS spectra of Pd-Ni/AC-LA catalyst. FT-IR spectra of AC and Pd-Ni/AC-LA catalysts. Top and side views of the Pd(111), Ni/Pd(111)-O, and Ni/Pd(111)-ON surfaces. Bader charge of Pd(111), Ni/Pd(111)-O, and Ni/Pd(111)-ON. The Pd loading in Pd/AC and Pd/AC-LA, as well as the coloading of Pd and Ni in Pd-Ni/AC and Pd-Ni/AC-LA. The structural properties of Pd-Ni/AC and Pd-Ni/AC-LA were characterized by N<sub>2</sub> adsorption–desorption isotherms. (PDF)

## AUTHOR INFORMATION

### Corresponding Authors

**Qian Lin** – School of Chemistry and Chemical Engineering, Guizhou Key Laboratory for Green Chemical and Clean Energy Technology, Guizhou University, Guiyang, Guizhou 550025, China;  [orcid.org/0000-0001-9770-3826](https://orcid.org/0000-0001-9770-3826); Email: [celinqianphy@163.com](mailto:celinqianphy@163.com)

**Hongyan Pan** – School of Chemistry and Chemical Engineering, Guizhou Key Laboratory for Green Chemical and Clean Energy Technology, Guizhou University, Guiyang, Guizhou 550025, China;  [orcid.org/0000-0002-0958-8985](https://orcid.org/0000-0002-0958-8985); Email: [cepanhongyan@163.com](mailto:cepanhongyan@163.com)

**Yongyong Shi** – School of Chemistry and Chemical Engineering, Guizhou Key Laboratory for Green Chemical and Clean Energy Technology, Guizhou University, Guiyang, Guizhou 550025, China; Email: [yyshi@gzu.edu.cn](mailto:yyshi@gzu.edu.cn)

**Donghai Jiang** – School of Chemical Engineering, Guizhou Institute of Technology, Guiyang 550003, China; Email: [dhjiang@git.edu.cn](mailto:dhjiang@git.edu.cn)

### Authors

**Xuan Chen** – School of Chemistry and Chemical Engineering, Guizhou Key Laboratory for Green Chemical and Clean Energy Technology, Guizhou University, Guiyang, Guizhou 550025, China

**Zheng Chen** – School of Chemistry and Chemical Engineering, Guizhou Key Laboratory for Green Chemical and Clean Energy Technology, Guizhou University, Guiyang, Guizhou 550025, China;  [orcid.org/0000-0002-6073-7288](https://orcid.org/0000-0002-6073-7288)

**Lang Wu** – School of Chemistry and Chemical Engineering, Guizhou Key Laboratory for Green Chemical and Clean Energy Technology, Guizhou University, Guiyang, Guizhou 550025, China

**Feifei Hu** – School of Chemistry and Chemical Engineering, Guizhou Key Laboratory for Green Chemical and Clean Energy Technology, Guizhou University, Guiyang, Guizhou 550025, China

**Xin Zhou** – School of Chemistry and Chemical Engineering, Guizhou Key Laboratory for Green Chemical and Clean Energy Technology, Guizhou University, Guiyang, Guizhou 550025, China

Complete contact information is available at:  
<https://pubs.acs.org/10.1021/acs.langmuir.5c00997>

## Notes

The authors declare no competing financial interest.

## ACKNOWLEDGMENTS

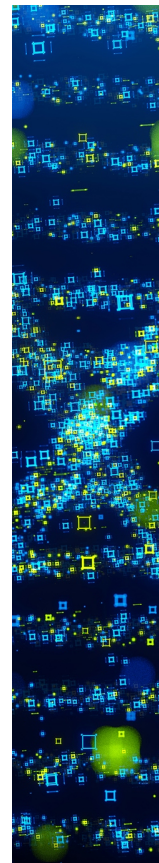
This work was financially supported by the Natural Science Foundation of China (No. 22068009 and 22262006), the Science and Technology Support Project of Guizhou Provincial Science and Technology Department (No. ZK[2023]050 and [2023]403), and the Guizhou Province Outstanding Young Scientific and Technological Talents Program (No. YQK2023007).

## REFERENCES

- (1) Campos-Martin, J. M.; Blanco-Brieva, G.; Fierro, J. L. G. Hydrogen Peroxide Synthesis: An Outlook beyond the Anthraquinone Process. *Angew. Chem., Int. Ed.* **2006**, *45* (42), 6962–6984.
- (2) Edwards, J. K.; Hutchings, G. J. Palladium and Gold-Palladium Catalysts for the Direct Synthesis of Hydrogen Peroxide. *Angew. Chem., Int. Ed.* **2008**, *47* (48), 9192–9198.
- (3) Edwards, J. K.; Freakley, S. J.; Carley, A. F.; Kiely, C. J.; Hutchings, G. J. Strategies for Designing Supported Gold-Palladium Bimetallic Catalysts for the Direct Synthesis of Hydrogen Peroxide. *Acc. Chem. Res.* **2014**, *47* (3), 845–854.
- (4) Blanco-Brieva, G.; Desmedt, F.; Miquel, P.; Campos-Martin, J. M.; Fierro, J. L. G. Direct Synthesis of Hydrogen Peroxide without the Use of Acids or Halide Promoters in Dissolution. *Catal. Sci. Technol.* **2020**, *10* (8), 2333–2336.
- (5) Tian, P.; Ding, D.; Sun, Y.; Xuan, F.; Xu, X.; Xu, J.; Han, Y.-F. Theoretical Study of Size Effects on the Direct Synthesis of Hydrogen Peroxide over Palladium Catalysts. *J. Catal.* **2019**, *369*, 95–104.
- (6) García-Serna, J.; Moreno, T.; Biasi, P.; Cocero, M. J.; Mikkola, J.-P.; Salmi, T. O. Engineering in Direct Synthesis of Hydrogen Peroxide: Targets, Reactors and Guidelines for Operational Conditions. *Green Chemistry*. **2014**, *16* (5), 2320.
- (7) Lewis, R. J.; Hutchings, G. J. Recent Advances in the Direct Synthesis of H<sub>2</sub>O<sub>2</sub>. *Chem. Cat. Chem.* **2019**, *11* (1), 298–308.
- (8) Yang, S.; Verdaguera-Casadevall, A.; Arnarson, L.; Silvioli, L.; Čolić, V.; Frydendal, R.; Rossmisl, J.; Chorkendorff, I.; Stephens, I. E. L. Toward the Decentralized Electrochemical Production of H<sub>2</sub>O<sub>2</sub>: A Focus on the Catalysis. *ACS Catalysis*. **2018**, *8* (5), 4064–4081.
- (9) Morandi, P.; Flaud, V.; Tingry, S.; Cornu, D.; Holade, Y. Tartaric Acid Regulated the Advanced Synthesis of Bismuth-Based Materials with Tunable Performance towards the Electrocatalytic Production of Hydrogen Peroxide. *Journal of Materials Chemistry A* **2020**, *8* (36), 18840–18855.
- (10) Cheng, Z.; Lippi, R.; Li, C.; Yang, Y.; Tang, L.; Huang, S.; Lee, W. J.; Lim, S.; Ma, X.; Patel, J. Experimental and Kinetic Study of the Direct Synthesis of Hydrogen Peroxide from Hydrogen and Oxygen over Palladium Catalysts. *Ind. Eng. Chem. Res.* **2019**, *58* (45), 20573–20584.
- (11) Alotaibi, F.; Al-Mayman, S.; Alotaibi, M.; Edwards, J. K.; Lewis, R. J.; Alotaibi, R.; Hutchings, G. J. Direct Synthesis of Hydrogen Peroxide Using Cs-Containing Heteropolyacid-Supported Palladium-Copper Catalysts. *Catal. Lett.* **2019**, *149* (4), 998–1006.
- (12) Han, G.-H.; Lee, S.-H.; Seo, M.; Lee, K.-Y. Effect of Polyvinylpyrrolidone (PVP) on Palladium Catalysts for Direct Synthesis of Hydrogen Peroxide from Hydrogen and Oxygen. *RSC Advances*. **2020**, *10* (34), 19952–19960.
- (13) Jin, Z.; Wang, L.; Zuidema, E.; Mondal, K.; Zhang, M.; Zhang, J.; Wang, C.; Meng, X.; Yang, H.; Mesters, C.; Xiao, F.-S. Hydrophobic Zeolite Modification for in Situ Peroxide Formation in Methane Oxidation to Methanol. *Science*. **2020**, *367* (6474), 193–197.
- (14) Kim, M.-C.; Han, G.-H.; Xiao, X.; Song, J.; Hong, J.; Jung, E.; Kim, H.-K.; Ahn, J.-P.; Han, S. S.; Lee, K.-Y.; Yu, T. Anisotropic Growth of Pt on Pd Nanocube Promotes Direct Synthesis of Hydrogen Peroxide. *Appl. Surf. Sci.* **2021**, *562*, 150031.
- (15) Xu, H.; Cheng, D.; Gao, Y. Design of High-Performance Pd-Based Alloy Nanocatalysts for Direct Synthesis of H<sub>2</sub>O<sub>2</sub>. *ACS Catalysis*. **2017**, *7* (3), 2164–2170.
- (16) Zhang, Y.; Sun, Q.; Guo, G.; Cheng, Y.; Zhang, X.; Ji, H.; He, X. Trace Pt Atoms as Electronic Promoters in Pd Clusters for Direct Synthesis of Hydrogen Peroxide. *Chem. Eng. J.* **2023**, *451*, 138867.
- (17) Edwards, J. K.; Solsona, B.; N, E. N.; Carley, A. F.; Herzing, A. A.; Kiely, C. J.; Hutchings, G. J. Switching off Hydrogen Peroxide Hydrogenation in the Direct Synthesis Process. *Science*. **2009**, *323* (5917), 1037–1041.
- (18) Gu, J.; Wang, S.; He, Z.; Han, Y.; Zhang, J. Direct Synthesis of Hydrogen Peroxide from Hydrogen and Oxygen over Activated-Carbon-Supported Pd-Ag Alloy Catalysts. *Catal. Sci. Technol.* **2016**, *6* (3), 809–817.
- (19) Freakley, S. J.; He, Q.; Harrhy, J. H.; Lu, L.; Crole, D. A.; Morgan, D. J.; Ntainjua, E. N.; Edwards, J. K.; Carley, A. F.; Borisevich, A. Y.; Kiely, C. J.; Hutchings, G. J. Palladium-Tin Catalysts for the Direct Synthesis of H<sub>2</sub>O<sub>2</sub> with High Selectivity. *Science*. **2016**, *351* (6276), 965–968.
- (20) Ding, D.; Xu, X.; Tian, P.; Liu, X.; Xu, J.; Han, Y.-F. Promotional Effects of Sb on Pd-Based Catalysts for the Direct Synthesis of Hydrogen Peroxide at Ambient Pressure. *Chin. J. Catal.* **2018**, *39* (4), 673–681.
- (21) Jiang, D.; Shi, Y.; Zhou, L.; Ma, J.; Yin, C.; Lin, Q.; Pan, H. Co-Enhanced Pd-Based Catalysts for Direct Synthesis of Hydrogen Peroxide: Insights from DFT Studies and Experimental Verification. *J. Alloys Compd.* **2024**, *1002*, 175265.
- (22) Wang, S.; Lewis, R. J.; Doronkin, D. E.; Morgan, D. J.; Grunwaldt, J.-D.; Hutchings, G. J.; Behrens, S. The Direct Synthesis of Hydrogen Peroxide from H<sub>2</sub> and O<sub>2</sub> Using Pd-Ga and Pd-In Catalysts. *Catal. Sci. Technol.* **2020**, *10* (6), 1925–1932.
- (23) Maity, S.; Eswaramoorthy, M. Ni-Pd Bimetallic Catalysts for the Direct Synthesis of H<sub>2</sub>O<sub>2</sub> - Unusual Enhancement of Pd Activity in the Presence of Ni<sup>+</sup>. *J. Mater. Chem. A* **2016**, *4* (9), 3233–3237.
- (24) Feng, Y.; Shao, Q.; Huang, B.; Zhang, J.; Huang, X. Surface Engineering at the Interface of Core/Shell Nanoparticles Promotes Hydrogen Peroxide Generation. *National Science Review*. **2018**, *5* (6), 895–906.
- (25) Freitas, L. F. de L. e; Puértolas, B.; Zhang, J.; Wang, B.; Hoffman, A. S.; Bare, S. R.; Pérez-Ramírez, J.; Medlin, J. W.; Nikolla, E. Tunable Catalytic Performance of Palladium Nanoparticles for H<sub>2</sub>O<sub>2</sub> Direct Synthesis via Surface-Bound Ligands. *ACS Catal.* **2020**, *10* (9), 5202–5207.
- (26) Lari, G. M.; Puértolas, B.; Shahrokhi, M.; López, N.; Pérez-Ramírez, J. Hybrid Palladium Nanoparticles for Direct Hydrogen Peroxide Synthesis: The Key Role of the Ligand. *Angew. Chem., Int. Ed.* **2017**, *56* (7), 1775–1779.
- (27) Wu, L.; Qin, H.; Zhou, S.; Luo, Z.; Xiao, Y.; You, H.; Lin, Q.; Pan, H.; Wang, K. Electronic Regulation and Hydrophobicity Improvement of the Palladium Active Site by Ionic Liquid to Achieve High Selectivity Direct Synthesis of Hydrogen Peroxide. *Chem. Eng. J.* **2023**, *474*, 145829.

- (28) Lewis, R. J.; Koy, M.; Macino, M.; Das, M.; Carter, J. H.; Morgan, D. J.; Davies, T. E.; Ernst, J. B.; Freakley, S. J.; Glorius, F.; Hutchings, G. J. N-Heterocyclic Carbene Modified Palladium Catalysts for the Direct Synthesis of Hydrogen Peroxide. *J. Am. Chem. Soc.* **2022**, *144* (34), 15431–15436.
- (29) Yang, J.; Lu, X.; Han, C.; Liu, H.; Gong, D.; Mo, L.; Wei, Q.; Tao, H.; Cui, S.; Wang, L. Glycine-Assisted Preparation of Highly Dispersed Ni/SiO<sub>2</sub> Catalyst for Low-Temperature Dry Reforming of Methane. *Int. J. Hydrogen Energy.* **2022**, *47* (75), 32071–32080.
- (30) Sapner, V. S.; Chavan, P. P.; Sathe, B. R. L-Lysine-Functionalized Reduced Graphene Oxide as a Highly Efficient Electrocatalyst for Enhanced Oxygen Evolution Reaction. *ACS Sustainable Chem. Eng.* **2020**, *8* (14), 5524–5533.
- (31) Jiang, S.; Yang, J.; Zhai, S.; Zhang, L.; Tu, R.; Yu, T.; Zhai, D.; Sun, L.; Deng, W.; Ren, G. Ambient Hydrogen Storage and Release Using CO<sub>2</sub> and an L-Arginine-Functionalized PdAu Catalyst via pH Control. *ACS Catal.* **2022**, *12* (22), 14113–14122.
- (32) Inoue, T.; Kikutani, Y.; Hamakawa, S.; Mawatari, K.; Mizukami, F.; Kitamori, T. Reactor Design Optimization for Direct Synthesis of Hydrogen Peroxide. *Chem. Eng. J.* **2010**, *160* (3), 909–914.
- (33) Inoue, T.; Schmidt, M. A.; Jensen, K. F. Microfabricated Multiphase Reactors for the Direct Synthesis of Hydrogen Peroxide from Hydrogen and Oxygen. *Ind. Eng. Chem. Res.* **2007**, *46* (4), 1153–1160.
- (34) Inoue, T.; Adachi, J.; Ohtaki, K.; Lu, M.; Murakami, S.; Sun, X.; Wang, D. F. Direct Hydrogen Peroxide Synthesis Using Glass Microfabricated Reactor - Paralleled Packed Bed Operation. *Chemical Engineering Journal.* **2015**, *278*, 517–526.
- (35) Kanungo, S.; Paunovic, V.; Schouten, J. C.; D'Angelo, M. F. N. Facile Synthesis of Catalytic AuPd Nanoparticles within Capillary Microreactors Using Polyelectrolyte Multilayers for the Direct Synthesis of H<sub>2</sub>O<sub>2</sub>. *Nano Letters.* **2017**, *17* (10), 6481–6486.
- (36) Yang, Z.; Wei, Z.; Zhou, S.; Bao, B.; Zhao, S.; Gong, F. Direct Thermal Catalytic Synthesis of Hydrogen Peroxide by Using Microchip Reactor. *Chem. Eng. J.* **2023**, *456*, 140915.
- (37) Kresse, G.; Hafner, J. *Ab Initio* Molecular Dynamics for Open-Shell Transition Metals. *Phys. Rev. B* **1993**, *48* (17), 13115–13118.
- (38) Kresse, G.; Furthmüller, J. Efficient Iterative Schemes for *Ab Initio* Total-Energy Calculations Using a Plane-Wave Basis Set. *Phys. Rev. B* **1996**, *54* (16), 11169–11186.
- (39) Perdew, J. P.; Burke, K.; Ernzerhof, M. Generalized Gradient Approximation Made Simple. *Phys. Rev. Lett.* **1996**, *77* (18), 3865–3868.
- (40) Blöchl, P. E. Projector Augmented-Wave Method. *Phys. Rev. B* **1994**, *50* (24), 17953–17979.
- (41) Kresse, G.; Joubert, D. From Ultrasoft Pseudopotentials to the Projector Augmented-Wave Method. *Phys. Rev. B* **1999**, *59* (3), 1758–1775.
- (42) Henkelman, G.; Jónsson, H. Improved Tangent Estimate in the Nudged Elastic Band Method for Finding Minimum Energy Paths and Saddle Points. *J. Chem. Phys.* **2000**, *113* (22), 9978–9985.
- (43) Henkelman, G.; Uberuaga, B. P.; Jónsson, H. A Climbing Image Nudged Elastic Band Method for Finding Saddle Points and Minimum Energy Paths. *J. Chem. Phys.* **2000**, *113* (22), 9901–9904.
- (44) Henkelman, G.; Jónsson, H. A Dimer Method for Finding Saddle Points on High Dimensional Potential Surfaces Using Only First Derivatives. *J. Chem. Phys.* **1999**, *111* (15), 7010–7022.
- (45) Xiao, P.; Sheppard, D.; Rogal, J.; Henkelman, G. Solid-State Dimer Method for Calculating Solid-Solid Phase Transitions. *Journal of Chemical Physics.* **2014**, *140* (17), 174104.
- (46) Tian, P.; Ouyang, L.; Xu, X.; Ao, C.; Xu, X.; Si, R.; Shen, X.; Lin, M.; Xu, J.; Han, Y.-F. The Origin of Palladium Particle Size Effects in the Direct Synthesis of H<sub>2</sub>O<sub>2</sub>: Is Smaller Better? *J. Catal.* **2017**, *349*, 30–40.
- (47) Hu, B.; Deng, W.; Li, R.; Zhang, Q.; Wang, Y.; Delplanque-Janssens, F.; Paul, D.; Desmedt, F.; Miquel, P. Carbon-Supported Palladium Catalysts for the Direct Synthesis of Hydrogen Peroxide from Hydrogen and Oxygen. *J. Catal.* **2014**, *319*, 15–26.
- (48) Tian, P.; Ouyang, L.; Xu, X.; Xu, J.; Han, Y.-F. Density Functional Theory Study of Direct Synthesis of H<sub>2</sub>O<sub>2</sub> from H<sub>2</sub> and O<sub>2</sub> on Pd(111), Pd(100), and Pd(110) Surfaces. *Chin. J. Catal.* **2013**, *34* (5), 1002–1012.
- (49) Abdel-Fattah, E.; Ogawa, D.; Nakamura, K. Oxygen Functionalization of MWCNTs in RF-Dielectric Barrier Discharge Ar/O<sub>2</sub> Plasma. *Journal of Physics D: Applied Physics.* **2017**, *50* (26), 265301.
- (50) Li, S.; Wang, Z.; Jia, J.; Hou, C.; Hao, X.; Zhang, H. Preparation of Hydroxyl and (3-Aminopropyl)Triethoxysilane Functionalized Multiwall Carbon Nanotubes for Use as Conductive Fillers in the Polyurethane Composite. *Polym. Compos.* **2018**, *39* (4), 1212–1222.
- (51) Lu, X.; Wang, D.; Wu, K.-H.; Guo, X.; Qi, W. Oxygen Reduction to Hydrogen Peroxide on Oxidized Nanocarbon: Identification and Quantification of Active Sites. *J. Colloid Interface Sci.* **2020**, *573*, 376–383.
- (52) Piao, L.; Liu, Q.; Li, Y.; Wang, C. The Adsorption of L-Phenylalanine on Oxidized Single-Walled Carbon Nanotubes. *Journal of Nanoscience and Nanotechnology.* **2009**, *9* (2), 1394–1399.
- (53) Kuznetsova, A.; Mawhinney, D. B.; Naumenko, V.; Yates, J. T.; Liu, J.; Smalley, R.E. Enhancement of Adsorption inside of Single-Walled Nanotubes: Opening the Entry Ports. *Chem. Phys. Lett.* **2000**, *321* (3–4), 292–296.
- (54) Coyle, J. P.; Johnson, P. A.; DiLabio, G. A.; Barry, S. T.; Müller, J. Gas-Phase Thermolysis of a Guanidine Precursor of Copper Studied by Matrix Isolation, Time-of-Flight Mass Spectrometry, and Computational Chemistry. *Inorganic Chemistry.* **2010**, *49* (6), 2844–2850.
- (55) Hsiao, M.-C.; Liao, S.-H.; Yen, M.-Y.; Liu, P.-I.; Pu, N.-W.; Wang, C.-A.; Ma, C.-C. M. Preparation of Covalently Functionalized Graphene Using Residual Oxygen-Containing Functional Groups. *ACS Appl. Mater. Interfaces.* **2010**, *2* (11), 3092–3099.
- (56) Wu, L.; Ni, B.; Chen, R.; Shi, C.; Sun, P.; Chen, T. Ultrafine PdAu Nanoparticles Immobilized on Amine Functionalized Carbon Black toward Fast Dehydrogenation of Formic Acid at Room Temperature†. *Nanoscale Adv.* **2019**, *1* (11), 4415–4421.
- (57) Wang, D.; Chen, L. Temperature and pH-Responsive Single-Walled Carbon Nanotube Dispersions. *Nano Letters.* **2007**, *7* (6), 1480–1484.
- (58) Park, J.-E.; Jang, Y.-S.; Bae, T.-S.; Lee, M.-H. Biocompatibility Characteristics of Titanium Coated with Multi Walled Carbon Nanotubes—Hydroxyapatite Nanocomposites. *Materials.* **2019**, *12* (2), 224.
- (59) Voogt, E. H.; Mens, A. J. M.; Gijzeman, O. L. J.; Geus, J. W. Adsorption of Oxygen and Surface Oxide Formation on Pd(111) and Pd Foil Studied with Ellipsometry, LEED, AES and XPS. *Surf. Sci.* **1997**, *373* (2–3), 210–220.
- (60) Leisenberger, F. P.; Koller, G.; Sock, M.; Surnev, S.; Ramsey, M. G.; Netzer, F. P.; Klötzer, B.; Hayek, K. Surface and Subsurface Oxygen on Pd(111). *Surf. Sci.* **2000**, *445* (2–3), 380–393.
- (61) Zhang, Y.; Liao, Y.; Shi, G.; Wang, W.; Su, B. Preparation, Characterization, and Catalytic Performance of Pd-Ni/AC Bimetallic Nano-Catalysts. *Green Process. Synth.* **2020**, *9* (1), 760–769.
- (62) Wu, Z.; Yan, S.; Ye, C.; Xu, S.; Guo, J.; Wu, J. Investigation of Pd<sub>2</sub>B- and NiB-Doped Pd-Ni/C Electrocatalysts with High Activity for Methanol Oxidation. *ACS Applied Energy Materials.* **2024**, *7* (9), 3916–3926.
- (63) Arrigo, R.; Schuster, M. E.; Abate, S.; Wrabetz, S.; Amakawa, K.; Teschner, D.; Freni, M.; Centi, G.; Perathoner, S.; Hävecker, M.; Schlögl, R. Dynamics of Palladium on Nanocarbon in the Direct Synthesis of H<sub>2</sub>O<sub>2</sub>. *Chem. Sus. Chem.* **2014**, *7* (1), 179–194.
- (64) Wu, Q.; Shen, C.; Liu, C. Amino Acid (Histidine) Modified Pd/SiO<sub>2</sub> Catalyst with High Activity for Selective Hydrogenation of Acetylene. *Appl. Surf. Sci.* **2023**, *607*, 154976.
- (65) Kaden, W. E.; Wu, T.; Kunkel, W. A.; Anderson, S. L. Electronic Structure Controls Reactivity of Size-Selected Pd Clusters Adsorbed on TiO<sub>2</sub> Surfaces. *Science.* **2009**, *326* (5954), 826–829.

- (66) Rivera-Cárcamo, C.; Gerber, I. C.; Del Rosal, I.; Guicheret, B.; Castro Contreras, R.; Vanoye, L.; Favre-Régillon, A.; Machado, B. F.; Audevard, J.; De Bellefon, C.; Philippe, R.; Serp, P. Control of the Single Atom/Nanoparticle Ratio in Pd/C Catalysts to Optimize the Cooperative Hydrogenation of Alkenes. *Catal. Sci. Technol.* **2021**, *11* (3), 984–999.
- (67) Sun, W.; Wu, S.; Lu, Y.; Wang, Y.; Cao, Q.; Fang, W. Effective Control of Particle Size and Electron Density of Pd/C and Sn-Pd/C Nanocatalysts for Vanillin Production via Base-Free Oxidation. *ACS Catalysis*. **2020**, *10* (14), 7699–7709.
- (68) Kim, Y.; Kim, S.; Ham, H. C.; Kim, D. H. Mechanistic Insights on Aqueous Formic Acid Dehydrogenation over Pd/C Catalyst for Efficient Hydrogen Production. *J. Catal.* **2020**, *389*, 506–516.
- (69) Ouyang, L.; Tian, P.; Da, G.; Xu, X.-C.; Ao, C.; Chen, T.; Si, R.; Xu, J.; Han, Y.-F. The Origin of Active Sites for Direct Synthesis of  $H_2O_2$  on Pd/TiO<sub>2</sub> Catalysts: Interfaces of Pd and PdO Domains. *J. Catal.* **2015**, *321*, 70–80.
- (70) Brun, M.; Berthet, A.; Bertolini, J. C. XPS, AES and Auger Parameter of Pd and PdO. *J. Electron Spectrosc. Relat. Phenom.* **1999**, *104* (1–3), 55–60.
- (71) Ao, C.; Tian, P.; Ouyang, L.; Da, G.; Xu, X.; Xu, J.; Han, Y.-F. Dispersing Pd Nanoparticles on N-Doped TiO<sub>2</sub>: A Highly Selective Catalyst for  $H_2O_2$  Synthesis. *Catal. Sci. Technol.* **2016**, *6* (13), 5060–5068.
- (72) Yoon, J.; Han, G.-H.; Lee, M. W.; Lee, S.-H.; Lee, S. H.; Lee, K.-Y. Amine Functionalization Derived Lattice Engineered and Electron Deficient Palladium Catalyst for Selective Production of Hydrogen Peroxide. *Appl. Surf. Sci.* **2022**, *604*, 154464.
- (73) Lee, S.; Jeong, H.; Chung, Y.-M. Direct Synthesis of Hydrogen Peroxide over Pd/C Catalyst Prepared by Selective Adsorption Deposition Method. *J. Catal.* **2018**, *365*, 125–137.
- (74) Ji, X.; Chen, D.; Peng, L.; Frison, F.; Valle, C. D.; Tubaro, C.; Zecca, M.; Centomo, P.; Ye, D.; Chen, P. Sustainable Direct  $H_2O_2$  Synthesis over Pd Catalyst Supported on Mesoporous Carbon: The Effect of Surface Nitrogen Functionality. *Catalysis Today*. **2021**, *376*, 1–8.
- (75) Cao, K.; Yang, H.; Bai, S.; Xu, Y.; Yang, C.; Wu, Y.; Xie, M.; Cheng, T.; Shao, Q.; Huang, X. Efficient Direct  $H_2O_2$  Synthesis Enabled by PdPb Nanorings via Inhibiting the O–O Bond Cleavage in  $O_2$  and  $H_2O_2$ . *ACS Catal.* **2021**, *11* (3), 1106–1118.
- (76) Cui, J.; Ren, D.; Tan, J.; Zhang, H.; Guo, Y.; Huang, L. Surface Modification by Amino Group Inducing for Highly Efficient Catalytic Oxidation of Toluene over a Pd/KIT-6 Catalyst. *ACS Omega*. **2022**, *7*, 39950.
- (77) Yang, T.; Yang, C.; Le, J.; Yu, Z.; Bu, L.; Li, L.; Bai, S.; Shao, Q.; Hu, Z.; Pao, C.-W.; Cheng, J.; Feng, Y.; Huang, X. Atomically Isolated Pd Sites within Pd-S Nanocrystals Enable Trifunctional Catalysis for Direct, Electrocatalytic and Photocatalytic Syntheses of  $H_2O_2$ . *Nano Res.* **2022**, *15* (3), 1861–1867.
- (78) Yang, Z.; Hao, Z.; Zhou, S.; Xie, P.; Wei, Z.; Zhao, S.; Gong, F. Pd-Sn Alloy Catalysts for Direct Synthesis of Hydrogen Peroxide from  $H_2$  and  $O_2$  in a Microchannel Reactor. *ACS Appl. Mater. Interfaces*. **2023**, *15* (19), 23058–23067.
- (79) Freakley, S. J.; Piccinini, M.; Edwards, J. K.; Ntaijua, E. N.; Moulijn, J. A.; Hutchings, G. J. Effect of Reaction Conditions on the Direct Synthesis of Hydrogen Peroxide with a AuPd/TiO<sub>2</sub> Catalyst in a Flow Reactor. *ACS Catal.* **2013**, *3* (4), 487–501.
- (80) Biasi, P.; Canu, P.; Menegazzo, F.; Pinna, F.; Salmi, T. O. Direct Synthesis of Hydrogen Peroxide in a Trickle Bed Reactor: Comparison of Pd-Based Catalysts. *Ind. Eng. Chem. Res.* **2012**, *51* (26), 8883–8890.
- (81) Biasi, P.; Menegazzo, F.; Pinna, F.; Eränen, K.; Salmi, T. O.; Canu, P. Continuous  $H_2O_2$  Direct Synthesis over PdAu Catalysts. *Chem. Eng. J.* **2011**, *176–177*, 172–177.
- (82) Rezaei, M.; Tabaan, S. H.; Haghshenas, D. F. Electrochemical Nucleation and Growth of Pd/PdCo Core-Shell Nanoparticles with Enhanced Activity and Durability as Fuel Cell Catalyst. *J. Mater. Chem. A* **2014**, *2* (13), 4588–4597.
- (83) Gul, S.; Nasim, F.; Iqbal, W.; Waseem, A.; Nadeem, M. A. High Performance Electrochemical  $CO_2$  Reduction over Pd Decorated Cobalt Containing Nitrogen Doped Carbon. *RSC Adv.* **2024**, *14* (19), 13017–13026.
- (84) Yang, X.; Yuan, S.; Guo, K.; Ni, H.; Song, T.; Lyu, W.; Wang, D.; Li, H.; Pan, S.; Zhang, J.; Zhao, J.-T. Achieving Low Lattice Thermal Conductivity in Half-Heusler Compound LiCdSb via Zintl Chemistry. *Small Science*. **2022**, *2* (12). DOI: [10.1002/smss.202200065](https://doi.org/10.1002/smss.202200065).
- (85) Louzguine, D. V.; Inoue, A. Electronegativity of the Constituent Rare-Earth Metals as a Factor Stabilizing the Supercooled Liquid Region in Al-Based Metallic Glasses. *Appl. Phys. Lett.* **2001**, *79* (21), 3410–3412.
- (86) Zhang, B.; Chou, L.; Bi, Y. Tuning Surface Electronegativity of BiVO<sub>4</sub> Photoanodes toward High-Performance Water Splitting. *Applied Catalysis B: Environment and Energy*. **2020**, *262*, 118267.
- (87) Han, G.-H.; Lee, S.-H.; Hwang, S.-Y.; Lee, K.-Y. Advanced Development Strategy of Nano Catalyst and DFT Calculations for Direct Synthesis of Hydrogen Peroxide. *Adv. Energy Mater.* **2021**, *11* (27). DOI: [10.1002/aenm.202003121](https://doi.org/10.1002/aenm.202003121).



CAS BIOFINDER DISCOVERY PLATFORM™

## STOP DIGGING THROUGH DATA — START MAKING DISCOVERIES

CAS BioFinder helps you find the right biological insights in seconds

**Start your search**